National University of Science and Technology Politehnica Bucharest

Doctoral School of Engineering and Applications of Lasers and Accelerators

Rareș Iovănescu

On phenomena in laser wakefield acceleration using PIC simulations

Ph.D. Thesis Summary

Supervisor
CS I Dr. Cătălin M. Ticoș

Bucharest, 2025

Contents

1 Motivation and thesis structure

In this thesis summary, we will provide the main ideas studied, both by reviewing the literature and by original contributions, and the thesis structure.

The aim of this research is to study the laser-plasma interaction, specifically, the laser wakefield acceleration (LWFA) mechanism and the radiation emission in this process by performing Particle-in-Cell (PIC) simulations. This acceleration mechanism was first theoretically proposed in 1979 [1] and experienced a significant scientific interest due to its applications, which may include the electron acceleration, as well as their x-ray emission, with various industrial applications and fundamental research. These accelerations take place over short lengths of millimeters to centimeters orders, and electrons reach GeV order energies, less costly than a classical radio frequency accelerator. We perform in this thesis a comprehensive study of its aspects, including the electron acceleration dynamics, the betatron radiation emitted by the electrons during their acceleration, and perform 2D PIC simulations in the EPOCH code and also approach the aspects of the computational simulation algorithm.

The thesis is structured in ten Chapters and an Appendix, and after the introduction in Chapter 1, it describes the electromagnetic waves in plasma in Chapter 2 and the laser wakefield acceleration in Chapter 3. In Chapter 4, we study the radiation emitted by a moving charge, and in Chapter 5, the PIC algorithm and the computational aspects of the laser-plasma simulations. Following these, we present our original contributions in the literature in the next four chapters, starting with the study on optimization the PIC simulations in Chapter 6, the modelling of the electron dynamics in LWFA using a central field in Chapter 7, the observed electron injection into filament structures in Chapter 8 and the LWFA mechanism in a periodic plasma density profile in Chapter 9. After these and the conclusions in Chapter 10, we provide in the Appendix more insights about calculations encountered by this point.

We will provide further the main aspects of the existing literature in this domain, establishing the foundations for our research.

2 Literature overview

In this chapter, we will describe the main theoretical foundations for our research, approached in Chapters 2-5, regarding the plasma-wave interaction, the laser wakefield acceleration mechanism, the radiation emitted by a moving charge, and, additionally, the computational simulations.

Electromagnetic waves in plasma

We study in Chapter 2 the EM waves propagation into plasma and their interaction. We first investigate the kinetic plasma description and obtain the Vlasov equation [2] from the Boltzmann equation without the collision term, which is also used in the PIC simulation algorithm to model the plasma distribution. This formula states that the total derivative with respect to time of the distribution function in phase space $f(\mathbf{x}, \mathbf{p}, t)$ equals zero. This distribution provides the probability per unit volume in phase space for a particle to position itself at the position $\mathbf{x}$ and having the momentum $\mathbf{p}$ at the time t.

We then study the dispersion relation of the electromagnetic waves in vacuum and in plasma. This relation bounds the angular frequency to the wavenumber. It is derived using Maxwell's equations, without the sources, ρ and $\mathbf{j}$ in the case of vacuum and with these sources present in the case of plasma, giving $\omega^2 = \omega_p^2 + k^2c^2$. This relation is needed for deriving the two velocities characteristic of a wave, namely the phase velocity, $v_\phi = \omega/k$ and the group velocity $v_g = \mathrm{d}\omega/\mathrm{d}k$. It is worth noting here that the phase velocity is only the rate of change of the phase and does not transport information, being in plasma larger than c. These velocities are further used in the formula of the refractive index, which can be defined as $n = c/v_\phi = \sqrt{\epsilon_0\mu_0}$. From here, we obtain the refractive index in plasma as $\sqrt{1 - \omega_p^2/\omega^2}$ and is less than one. It is also observed that in this case $v_\phi v_g = c^2$.

Using these, we then investigate the self-focusing of the laser due to the Kerr effect, which happens when a highly intense pulse modifies the nonlinear refractive index in a medium, creating a lower index at the pulse margins compared to the center. The refraction of the waves on these successive layers of smaller refractive index may lead to them compensating for the natural diffraction of the laser, thus

keeping it focused. We derived here the power necessary for the Kerr effect to occur, and how the refractive index is changed due to the nonlinear terms of the polarization density.

Laser Wakefield Acceleration

In Chapter 3, we study the fundamental aspects of the laser wakefield acceleration mechanism. This starts with the ponderomotive force of the laser field that entered the plasma. This force expels the electrons towards the pulse margins and creates, behind the laser, an electron-free cavity, usually called bubble. The electrons can be trapped in this structure by the attractive potential of the ionic field in the bubble and then accelerated to high energies. We derived first the ponderomotive force in both the relativistic and non-relativistic cases. This force is averaged over a laser cycle $2\pi/\omega$, and in both cases is independent of the charge sign of the particles, expelling them from areas of stronger field to weaker field, independently of their charge sign. Its relativistic value for an electron is derived as $-mc^2\boldsymbol{\nabla}\gamma$, while the Lorentz factor can be further expressed from the laser magnetic potential.

Following these, we studied several parameters of the laser, significant for the LWFA mechanism, such as the laser intensity, which is the average of the Poynting vector of the laser. The intensity is obtained as $I = \epsilon_0 c E_0^2/2$, and the factor 2 is the result of averaging over the harmonic period of the field. Another important parameter is the normalized vector potential of the laser, which is $a = eA/(mc)$. This gives the maximum momentum transferred from the laser to the electron, and can also be used in the formula of the relativistic ponderomotive force to express the Lorentz factor.

This acceleration mechanism has, however, several limitations. We describe further two of them, namely the dephasing and the pump depletion. The former one limits the electron acceleration after the electron passes approximately half of the bubble length, meaning that more positive charge remains behind it than in front of it. Thus, the electric field will change its sign at that point and the electron will experience deceleration. The total acceleration distance until the electron reaches the midpoint of the bubble is known as the dephasing length. The other limitation is given by the pump depletion length. This arises due to the fact that the frontal part of the pulse will experience a higher density plasma before the electrons are expelled, and thus a lower refractive index and a lower group velocity than the rest of the pulse. Moreover, the frontal part transfers energy to the plasma, gradually reducing the beam's energy. The difference between the group velocity and the slower frontal velocity is known as the etching velocity and is approximately $c\omega_p^2/\omega^2$. After the rear part of the pulse travelling at this speed, relative to the frontal part, catches up with the front, the laser will be depleted,

and the LWFA mechanism will no longer occur. The distance over which the electron is accelerated in this time is known as the pump depletion length.

We then examined the electron self-injection in the bubble, which is the necessary condition for them to experience acceleration. The condition for the electron to be trapped in the attractive potential of the ionic bubble will be that its Hamiltonian, $H < 0$. The electron Hamiltonian can be written as $H = \gamma mc^2 - e\phi - v_0 P_x$, where v_0 is the bubble velocity, P_x the canonical momentum of the electron in this direction and ϕ the electric potential. This calculation was detailed in the Appendix, where we derived the Lagrangian and Hamiltonian of a relativistic electron using a generalized potential, as the Lorentz force is not conservative. From here, we obtained the Hamiltonian equations of the derivatives with respect to time of the positions and the canonical momenta, as functions of the electric and magnetic potential. This can be solved to obtain several plots of their trajectories for given conditions. Following this, we derived the electron acceleration in a spherical bubble and examined for which laser and plasma parameters the dephasing or the depletion are more constraining limitations. We then investigated the self-focusing mechanism of the laser in plasma. There are several causes of this, and they all act synergetically. These are the thermal effects, parts of the plasma experience an adiabatic expansion due to the interaction with the laser, and thus reduce the density and increase the refractive index. The other two effects are the ponderomotive and relativistic self-focusing, where a density gradient of the expelled electrons is created by the ponderomotive force, and where the relativistic increase of mass modifies the plasma angular frequency. The formula or the refractive index is given by

$$n = \sqrt{1 - \frac{n_e}{\gamma n_c}}\,. \tag{2.1}$$

We analyzed these last two effects using a Vlasov model [3] with a distribution function and the action of the ponderomotive force and the charge separation force in plasma.

Radiation by a moving charge

The accelerated electrons experience transverse oscillations in their motion in the bubble and thus emit synchrotron-like radiation, known in this case as betatron radiation. We examine the radiation emitted by moving charges in Chapter 4. We start with the Larmor formula, which gives the radiation power emitted by an accelerating charge moving in a straight line. The main idea of this derivation is to obtain the transversal component of the electric field, which is caused by the acceleration. Using this, the Poynting vector is obtained, and by integrating it over the solid angle, we obtain the power radiated, which is given as $P = a^2 q^2/(6\pi\epsilon_0 c^3)$. This shows that the radiation emission does not depend on the sign of both the

acceleration and the charge. This formula was, however, derived before the theory of relativity; hence, it does not contain the effects of acceleration at high velocities.

For solving this, a specific case of the retarded potentials, for moving point-like charges, is used, namely the Liénard–Wiechert potentials. Their derivation starts with the retarded time, which is the time when an electromagnetic field began to propagate with c towards an observation point. Using this retarded time and the Lorentz gauge, the retarded potentials and fields are further derived. Having the fields also gives the Poynting vector, and thus, the power radiated at the retarded time is obtained by integrating it over the solid angle and dividing by the derivative of the retarded time with respect to time. Using this, a generalization of the Larmor formula for the relativistic case, known as Liénard's formula, was derived, showing that the power radiated depends on a γ^6 factor. This motion was studied on an arbitrary trajectory of the particle. If the trajectory is curved, the emitting radiation is known as synchrotron radiation. Because in the case of circular motion with the same speed v, the acceleration has only the radial component v^2/r, it is obtained that the power radiated in the circular motion compared to the one emitted in a linear motion, under the same force and particle, will be large with a factor of γ^2 for the circular motion. We further derived the spectrum of the emitted photons by pursuing a Fourier transform and obtaining the electric field as a function of angular frequency. We also obtained the angular and angular frequency distributions of the emitted photons' energies, also introducing the critical frequency, which gives the position above which half of the power is emitted, and half is emitted below it.

This description of the radiation was necessary for the study of the betatron radiation obtained in LWFA, which is a synchrotron-like radiation. The injected electrons in the bubble of LWFA perform transverse oscillations, called betatron oscillations. Thus, their accelerated motion on a sinusoidal trajectory will lead to the betatron radiation emission. Due to the acceleration and, thus, the relativistic increase of mass, the oscillation amplitude decreases in time, while the wavelength increases. The main parameter describing this regime is called the wiggler strength parameter and is given by $K = \gamma v_\perp / c$, where $v_\perp$ is the maximum electron transversal velocity, achieved on the horizontal axis. These oscillations are divided into two regimes: undulator, with $K \ll 1$ and wiggler, where $K \gg 1$.

The radiation is emitted forward in a cone with the half angle $\theta = 1/\gamma$ in the case of the undulator regime and with $\psi = K/\gamma$ for the wiggler regime. The angular frequency of these oscillations also decreases with the Lorentz factor as $\omega_\beta = \omega_p/\sqrt{2\gamma}$. Approximating the trajectory with a sinusoid, the minimum curvature radius is obtained at the maximum transverse position and its value is given by $\rho_0 = \lambda_u \gamma/(2\pi K)$, where λ_u is the wavelength of the betatron oscillation of the electrons. The critical frequency is obtained for this radius as, $\omega_c = 3c\gamma^3/(2\rho_0)$.

Other parameters derived for the radiation emitted are the average power and energy radiated the number of photons emitted per electron per oscillation cycle.

Computational simulations

In Chapter 5, we study the computational simulations, with the PIC algorithm and the finite-difference time-domain (FDTD) method. In the PIC algorithm of modelling the plasma dynamics, collections of particles are replaced with fewer macroparticles, which have an assigned weight, that is, the number of real particles per simulation macroparticle. The space and time are both discretized, using a grid for the space, and we will consider the case of a Cartesian grid. The electric and magnetic fields, along with the current and charge densities, are derived on the grid points, most often using the FDTD method.

There are several variants of FDTD. The original one was proposed by K. Yee in 1966 [4] and updates the electric fields at integer grid steps and the magnetic fields at half-integer (leapfrog algorithm). Other variants, like the one used in the EPOCH code, derive the fields at both integer and half-integer positions. These are obtained successively from Maxwell's equations, as the derivative on a discretized grid is written as

$$\left(\frac{\partial E_y^n}{\partial x}\right)_{i+\frac{1}{2},j,k} = \frac{E^n_{y_{i+1,j,k}} - E^n_{y_{i,j,k}}}{\Delta x}\,, \tag{2.2}$$

where the indeces (i, j, k) denote the spatial directions and n the time step. This is a central difference derivation and has only second-order errors, while the forward and backward differences have first-order errors. Thus, it is the most accurate derivative in this method. A necessary condition for the consistency of the FDTD method is to establish boundary conditions. We derived the absorbing boundary conditions, named Silver-Müller, which ensure the exit of EM waves from the simulation window, eliminating reflection.

We studied further the PIC algorithm and its loop of updating the positions and velocities of the particles on the grid. This loop consists of four steps: firstly, the interpolation of the fields at the initial positions of the particles, then the particle pusher, updating their positions and velocities using the Lorentz force, followed by the current deposition, to obtain the current and charge densities on the grid, and the Maxwell solver to obtain the fields.

We described the PIC loop's four steps, starting with the particle pusher. Here, several algorithms have been proposed, with the Boris push [5] being the most used to this day. This is a second-order leapfrog integrator, and its idea is to split the linear acceleration due to the electric field in two and implement the rotation caused by the magnetic field between them. We derived this algorithm, both

relativistic and non-relativistic, obtaining the updated velocity after a time step from the Lorentz force.

Several improvements were proposed over time to mitigate the limitations encountered with the Boris algorithm. Despite its accuracy, in the relativistic case, the Boris pusher experiences inaccuracies in the case of the drift velocity. Specifically, when the Lorentz force cancels, $\mathbf{E} + \mathbf{v} \times \mathbf{B} = \mathbf{0}$, but the fields are non-zero, the algorithm gives numerical errors. To overcome this, the Vay pusher [6] was proposed, which derives a correct drift velocity. The main difference in the case of this algorithm is that for $\mathbf{E}^{n+1/2} + \mathbf{v}^n \times \mathbf{B}^{n+1/2} = \mathbf{E}^{n+1/2} + \mathbf{v}^{n+1} \times \mathbf{B}^{n+1/2} = \mathbf{0}$ and $\gamma^{n+1}\mathbf{v}^{n+1} = \gamma^n \mathbf{v}^n$ it derives correctly the electromagnetic fields. The velocity used for the Lorentz force does not contain in this case the Lorentz factor, which leads to lower error at high velocities compared to the Boris algorithm. Thus, this pusher ensures better accuracy at higher Lorentz factors and derives better the drift velocity, however, it is more computationally costly than the Boris algorithm. Still, a problem that arises is that the Vay pusher is not volume preserving in phase-space, which is a condition for Hamiltonian systems according to Liouville's theorem, while Boris algorithm, despite not being symplectic, preserves the volum and thus the error does not increase over the iterations.

To improve the advances made by the Vay pusher, a more recent pusher was proposed, named Higuera-Cary [7]. This pusher has the correct drift velocity, as proposed by Vay, and is also volume-preserving, like the Boris method. Although the most computationally costly among these psuhers, it is the most accurate one. We further demonstrated that the Boris pusher, despite not being symplectic, is volume-preserving in phase space, a property we also verified for the Higuera-Cary pusher. This happens when the Jacobian determinant of their transformation is one. This transformation is given by the updating of the positions and velocities at each iteration, $(\mathbf{x}_k, \mathbf{v}_k) \rightarrow (\mathbf{x}_{k+1}, \mathbf{v}_{k+1})$.

Before describing the next step of the PIC algorithm, which is the current deposition, we described the quasi-particle shape functions which are used to achieve this. The PIC codes model the plasma dynamics using the Vlasov-Maxwell equations; thus, the distribution function of the macroparticles is necessary. This function is written as

$$f(\mathbf{x}, \mathbf{p}, t) = \sum_{p=1}^{N_s} \frac{w_p}{V_c} S(\mathbf{x} - \mathbf{x}_p(t)) \delta(\mathbf{p} - \mathbf{p}_p(t)) \,, \tag{2.3}$$

where $S(\mathbf{x} - \mathbf{x}_p(t))$ is the shape function for the position and $\delta(\mathbf{p} - \mathbf{p}_p(t))$ gives the momentum distribution. Here, w_p is the particle's weight and V_c the cell hypervolume. This shape function is normalized to the cell hypervolume, and it can be of several orders for increased accuracy. We provided the expressions for the first four shape functions and a graphical representation of them. They are

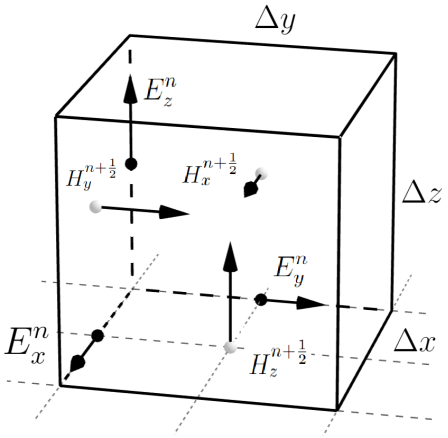

Figure 2.1: Representation of the electric and magnetic field on Yee's staggered grid.

based on the basis spline functions (b-spline) and also use the grid size length. Using these functions, it is now possible to obtain the current densities on the grid, which are derived with an algorithm proposed by Esirkepov [8]. A quantity used in this case is $W_p = qw_p/V_c$, which is the weight of the charge density and gives the total charge in a cell.

The next step in the PIC loop is the Maxwell Solver. This aims to solve the Maxwell-Faraday and Maxwell-Ampère equations with the FDTD method, using the previously obtained positions, velocities and current densities. Among the several Maxwell Solvers available, we will describe the most used one, the algorithm of Yee and the algorithm proposed by Pukhov. The Yee's method discretizes the space and time and writes a function of these four variables as

$$F(i\Delta x, j\Delta y, k\Delta z, n\Delta t) = F^n(i, j, k)\,. \tag{2.4}$$

The grid is represented in Fig. 2.1 showing how the electric and magnetic fields are calculated at positions at half-iteration distance. From here, it discretizes the Maxwell's equations for all three spatial directions. This method uses a staggered grid that derives the electric fields at integer positions and the magnetic fields at half-integer positions. We provided a 3D representation of the positions of the fields in this grid. Hence, by solving these dicretized equations, we obtain the electric and magnetic fields at the next time step, using their value at the previous one. The other Maxwell Solver algorithm that we describe is the Pukhov algorithm [9]. Among the improvements compared to Yee's algorithm is the reduction of the numerical dispersion along the axis with the smallest grid interval, and it also gives a higher accuracy order. These are achieved by using a modified FDTD discretization method, which multiplies the electric fields in the discretized

Maxwell-Faraday equations by four coefficients which depend on the grid step. Another difference is the modified magnetic interpolation, which is generally given at a half-integer position as the average of the magnetic fields on the integer positions near it. Pukhov's algorithm gives a more accurate four-point interpolation, which writes the magnetic field as

$$B_{i+\frac{1}{2},j} = a(B_{i,j} + B_{i+1,j}) + b(B_{i-1,j} + B_{i+2,j})\,, \tag{2.5}$$

with the constants $a + b = 0.5$. These parameters are computed in dependence on the grid step size and the wavelength.

The last of the four steps of the PIC loop is the field interpolation. This step aims to interpolate the fields at the particle's positions in the cells, using the fields derived on the grid. This is done with the shape function as,

$$\mathbf{E}_p^n = \frac{1}{V_c}\int \mathrm{d}^3\mathbf{x} S(\mathbf{x} - \mathbf{x}_p^n)\mathbf{E}^n(\mathbf{x})\,, \qquad \mathbf{B}_p^n = \frac{1}{V_c}\int \mathrm{d}^3\mathbf{x} S(\mathbf{x} - \mathbf{x}_p^n)\mathbf{B}^n(\mathbf{x})\,, \tag{2.6}$$

and here, as described before, the magnetic field is usually interpolated at a half-integer position as the average of the field on the two neighbouring integer positions.

We describe after this, the Courant–Friedrichs–Lewy condition (CFL), which ensures the numerical stability in the FDTD algorithm. The idea of this constraint is that the fields should be updated on the grid faster than the wave can reach that position. Otherwise, numerical artefacts will appear. Using the maximum wave speed, c, this condition bounds the grid and time steps and is written in 1D as $\Delta t \leq \Delta x/c$, where we used the grid and time intervals. In the 2D grid, this condition can be viewed as $\Delta t \leq h/c$, where h is the height in the square triangle with the catheti Δx and Δy. Thus, the slowest numerical speed, for the shortest distance, for an obliquely propagating wave has to be larger than c. Similarly, in the 3D case, this distance corresponds to the height in the triangular pyramid, formed from an origin point and its bases given by the three neighbouring grid points, at the distances Δx, Δy and Δz. We showed figures of these distances in both 2D and 3D. This condition is written in general as

$$\Delta t \leq \frac{1}{c\sqrt{\frac{1}{\Delta x^2} + \frac{1}{\Delta y^2} + \frac{1}{\Delta z^2}}}\,. \tag{2.7}$$

Another way to derive this condition is by using the discretized wave equation for the FDTD grid, which is

$$\frac{1}{c^2}\frac{\mathbf{E}^{n+1}_{a,b,c} - 2\mathbf{E}^{n}_{a,b,c} + \mathbf{E}^{n-1}_{a,b,c}}{\Delta t^2} = \frac{\mathbf{E}^{n}_{a+1,b,c} - 2\mathbf{E}^{n}_{a,b,c} + \mathbf{E}^{n}_{a-1,b,c}}{\Delta x^2} + \frac{\mathbf{E}^{n}_{a,b+1,c} - 2\mathbf{E}^{n}_{a,b,c} + \mathbf{E}^{n}_{a,b-1,c}}{\Delta y^2} + \frac{\mathbf{E}^{n}_{a,b,c+1} - 2\mathbf{E}^{n}_{a,b,c} + \mathbf{E}^{n}_{a,b,c-1}}{\Delta z^2}\,. \tag{2.8}$$

And by replacing the field with the plane wave profile of

$$\mathbf{E}^{n}_{a,b,c}(\mathbf{x}, t) = \mathbf{E}_0 \exp(i(k_x a\Delta x + k_y b\Delta y + k_z c\Delta z - \omega n\Delta t))\,, \tag{2.9}$$

the CFL condition will be obtained again after the derivations.

Having now established a description of the PIC simulation algorithm, we now focus on the existing PIC codes, especially on the EPOCH code [10], which we use in our simulations. Among other PIC codes, there are SMILEI, FBPIC, OSIRIS, and PICCANTE, and these are also open-source and freely available. The EPOCH code is written in Fortran and uses SI units for the physical quantities, which are separated into blocks in the code. We further described the most important blocks in this code. One of them is the control block, where grid quantities, the time step and simulation window dimensions are specified. The species block gives the information for one type of particle, and there are two in the case of plasma, for electrons and ions, but it may also contain one for photons if quantum electrodynamics effects are included. Here, their charges, masses and number densities are given. The laser block gives the laser parameters, its spot, wavelength, focusing position, and temporal profile and duration. Other blocks give the information for the boundaries and their conditions, or the moving simulation window and its velocity. The code also uses compiler flags, which may change several features of the code, such as a higher-order shape function, or choosing the Higuera-Cary pusher instead of Boris or changing the Maxwell Solver.

We will refer now mostly to the contributions to literature made for this thesis.

3 Research contributions

In This Chapter, we will focus on our contributions to the literature, consisting of four studies. Namely, about the optimization of the PIC simulations, the modelling of electron dynamics with a relativistic central field in LWFA, the observation of the electron filament structures formed in LWFA, and the LWFA mechanism in a periodic plasma density profile.

Optimization of PIC simulations for LWFA

In the first study [11], we investigated the optimization of the PIC simulation parameters for LWFA simulations. We aimed here to observe how the changes in the grid step sizes in the vertical and horizontal directions will impact the accelerated electrons' energies. For this, we performed 2D PIC simulations of LWFA in the EPOCH code, keeping the laser and plasma parameters constant and only varying the number of grid points. The aim of this study is to obtain a useful balance between accuracy, which increases with the number of grid points, and the computational power, which also increases. The dimensions of the moving simulation window were also kept constant and were $\Delta X = 230\lambda$ and $\Delta Y = 78\lambda$, where $\lambda = 0.8\,\mu\text{m}$ is the laser wavelength. In our first set of simulations, we varied the number of grid points in the horizontal direction (nx), having the values 3300, 3600, 3900 and 4100. We measured in each case the maximum electron energy evolution at intervals of 250 fs. We observed that the energy grows with the increase in the number of cells in the horizontal direction and approaches a convergence zone. We presented for each case the graphs of these energies and the maps of the number density and electron energy distribution.

Following these results, we varied the number of cells on the vertical grid (ny), having the values 700, 900, 1000, 1100, and keeping constant all the other parameters. In this case, however, the results showed a decrease in energy for the higher number of cells and approached again a convergence zone. In the next set of simulations, we chose different values for the number of particles per cell, specifically, 4 electrons and 2 ions, in the first case, 6 electrons and 3 ions, in the second case and 8 electrons and 4 ions in the last case. This is done because we used Helium

plasma with the ion density half of the electron's. The code will, however, give the same density using the same weighting scheme $w_p = nV_c/N$ and thus, our results showed minimal changes. Hence, a lower number of particles per cell in the simulations will have negligible impact on its result and will reduce the computational power demanded. In our last set of simulations, we varied the number of grid cells in both directions while keeping the cell in a square form. In this case, the accelerated electrons' energies increased with the number of cells. We showed in each case the graph of electron energy variation.

We further analyzed the impact of the number of cells variation on the accuracy of the Boris algorithm used here. As described before, the Boris algorithm splits in two the linear acceleration due to the electric field and adds in between the rotation given due to the magnetic component. Due to the CFL condition, for a smaller grid step, the time step will also decrease, thus the angle of the Boris rotation will be lower and give a more exact derivation. This condition for the stability of the angle of Boris rotation was derived as $\Delta t \ll \lambda/(a_0 c)$ [12]. However, it is less restrictive than the CFL in our case, and also not so strict in LWFA compared to direct laser acceleration, where the electron enters the areas of the strongest field.

We also approached the issue of computational optimization, studying the number of MPI processes for such simulations to be performed in the least time. The results showed the minimum computational time obtained for 14 MPI processes for our PIC simulations using EPOCH.

Thus, we investigated in this study the impact of varying the number of cells on both directions and particles per cell on the electron energy, as well as the number of MPI processes for the minimal computational time used. These provide the insights for choosing the appropriate balance between accuracy and computational resources.

Electron dynamics in LWFA with a relativistic central field approach

In our second study [13], we investigated the trajectories of the electrons forming the bubble of the LWFA. We modelled these trajectories with an attractive central field, considering the bubble charge placed in its center and the electrons being deviated by its action. Thus, the electrons will experience a trajectory characteristic of a central field motion. We observe two cases of dynamics. One, when the minimum radius in this trajectory is above the horizontal axis, resulting in the electrons closing the bubble, will point towards the exterior. In the other case, this minimum radius is reached below the axis and will make the electron point towards the interior of the bubble, resulting in a direct injection.

Thus, we performed the calculations for this central field model, deriving the minimum radius and its polar angle where it is obtained. This was done by writing

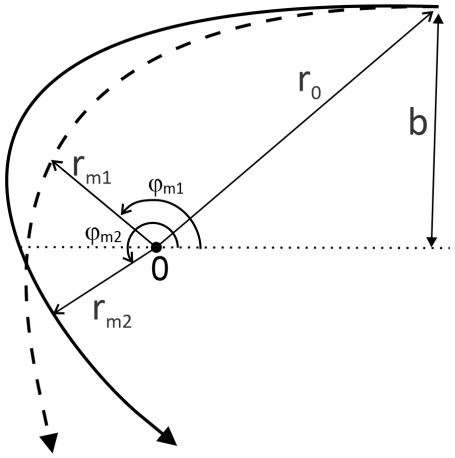

Figure 3.1: Representation of the two possible trajectories modelled with a relativistic central field.

the conservation of energy and angular momentum in this relativistic motion. We worked with polar coordinates of (r, ϕ) and the minimum radius was obtained when $\dot{r} = 0$, which is its time derivative. And after obtaining the formulas for both $\dot{r}$ and $\dot{\phi}$, we derived the angle in the case of the minimum radius, obtaining less than π when it is above the axis and larger than π when it is reached below the axis.

We exemplified thorough simulations these two cases and calculated these values for the given parameters. We also compared the evolution of the maximum electron energies for both cases and presented the graphical representation, showing larger energies for the bubble with the minimum radius obtained above the axis, for which a larger plasma density was used. We performed these simulations using the CFL condition at 0.8 of the maximum value possible. The two trajectories are shown in Fig. 3.1, showing the polar angle less than π when the minimum radius is above the axis, and larger than π when it is below the axis.

Thus, we proposed in this study an analytic model for the electron dynamics in LWFA and verified it through 2D PIC simulations, observing the particularities of the bubble formation.

Electron filament structures of injected electrons in LWFA

In the third study [14], we continued the investigation of the different bubble shapes obtained in LWFA and also concerning the different effects arising from this.

Thus, we performed 2D PIC simulations in EPOCH, keeping all parameters constant and varying only the plasma density, which reaches 6 values, 0.9, 1, 1.5, 2,

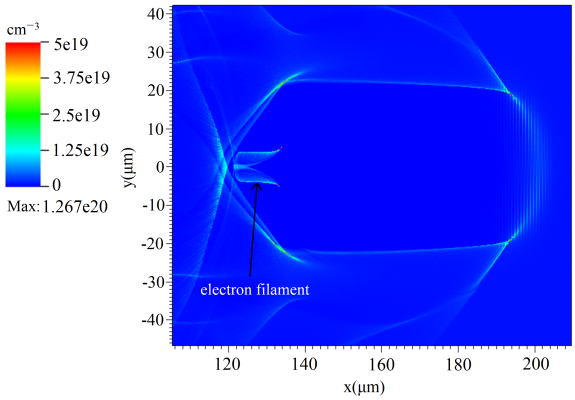

Figure 3.2: The formation of the electron filament structures after a simulation time of 700 fs for the plasma density $9 \times 10^{17}\,\mathrm{cm}^{-3}$.

2.5 and $4 \times 10^{18}\,\mathrm{cm}^{-3}$. We observed how, for the first four densities, the bubbles are larger, and the electrons close them, pointing towards the interior, at the bubble rear. This makes an angle larger than π at their closure, measured from the interior of the bubble. Conversely, for the last two densities, the smaller bubbles, formed after a shorter time, will close under an angle less than π. This results in a different injection of the electrons and further in different betatron oscillations. We measured in all the cases, this angle of bubble closure and the bubble formation time, as well as showing the electron energy distribution map obtained from the simulations. We referred to the electron-injected structures as electron filament structures and showed their formation and evolution in the bubble in Fig. 3.2 after a simulation time of 700 fs. We further plotted trajectories resembling these cases by solving the Hamiltonian equations with the Runge-Kutta 4 algorithm. We obtained a trajectory for both injection cases, towards the interior and exterior of the bubble.

After this, we investigated how the betatron oscillation parameters are influenced by this different injection. The main difference was a larger oscillation amplitude for smaller densities, where the electrons were injected towards the interior. We measured the Lorentz factor at the midpoint of the oscillation, which gave, however, larger values for the higher densities. This is due to the fact that the stronger electric field in a bubble formed at higher plasma density will accelerate stronger the electrons compared to a bubble at lower density, despite being smaller at high densities. Thus, the wiggler strength, which grows with the oscillation amplitude r and with $\sqrt{\gamma}$, will increase with the density, reaching the highest values at the fifth density. In the case of the angle of radiation emission, which is obtained as K/γ, there was a decrease with the plasma density, mainly due to the larger amplitude at the lowest densities. We also measured the critical energy

in these cases, which is given by $E_c = 3K^3\hbar\gamma_z^2\omega_\beta/4$, where we used the average Lorentz factor in the longitudinal direction. This is observed to grow with the density, and so does the number of emitted photons per electron per oscillation cycle, which we also measured. Another parameter that we measured was the oscillation wavelength, which increases in the last two cases, where the bubble closes towards the interior, mainly due to a larger acceleration at the higher densities. Using this, we also derived the average radiated power and energy per oscillation cycle. They experience both a growth in the case of the last two densities.

Lastly, we investigated how the bubble formation and the electron injection are modified using a plasma density upramp at the start of the simulation. We chose a density profile of the type $n_0 x/x_0$, for $x_0 < x$ and n_0 after this, in our case, $2 \times 10^{24}\,\mathrm{cm}^{-3}$, and performed three simulations with the values of x_0 5, 10 and 20 µm. The effect observed is that the bubble angle of closure becomes smaller with the increase of the upramp distance. The bubble already closes with an angle less than π for the second upramp distance. We measured in this case also the parameters of the betatron oscillations, observing that the oscillation amplitude decreases with the upramp, while the betatron wavelength increases. Due to the increase in the Lorentz factor for lower upramps, as the injection is delayed by the electron trapping in the bubble sheath, and we take the Lorentz factor at the midpoint of the oscillation, the power and energy radiated will increase with the upramp. The wiggler strength parameter, however, will experience small variations.

Thus, in this study, we examined how the bubble geometry is influenced by plasma density and profile and what consequences this has on the betatron oscillations. These constitute a comprehensive analysis of how the betatron radiation parameters change when the bubble formation is different.

LWFA in periodic plasma density profile

In our fourth study [15], we approached the case of LWFA in a periodically modulated plasma density profile. We chose a plasma density profile of the type $n(x) = n_0(1 + \delta \sin 2\pi x/x_0)$, and performed simulations for the modulation parameter δ taking the values 0, 0.1, 0.3, 0.5, 0.7. We presented the electron energy distribution maps for each case and measured the maximum electron energy evolution, observing a decrease in energy with the increase in the modulation.

We then derived a model of the electron acceleration in a bubble of varying size, formed in this modulated density, and observed that the centre of the bubble will oscillate around to the maximal position, the center of the largest bubble formed at the minimum density and the center of the smallest one, formed at the maximum density. We compared this result with the energy spectrum of the electrons that we plotted and showed convergent results. Following this, we derived the dephasing

and depletion lengths for this periodic profile by performing their average over the modulated density and then compared how both of them vary with the modulation parameter. We observed that the depletion will be a more significant limitation, as the dephasing is mostly mitigated by this modulated profile. In deriving both the electron energy and these lengths, we encountered a special integral, whose derivation we detailed in the Appendix. This has the general form

$$I = \int_0^L \frac{\mathrm{d}x}{1 + D\sin(ax)}\,, \tag{3.1}$$

and because its primitive is also a periodic function, it is solved with the half-tangent substitution method, and we approached all its aspects and applied it to our particular case.

We also measured the parameters of the betatron radiation for the modulated profiles. The oscillation amplitude is observed to increase with the modulation parameter and also the total angle of radiation emission ψ and the wiggler strength parameter. The average radiated power and energy have oscillating values, with the maximum obtained for energy at $\delta = 0.3$ and for the power at $\delta = 0.1$.

Besides this, we also calculated the transversal emittance of the injected electron bunches in all the cases using a code in Python, which extracted the vertical position (y) and the momentum components, p_x and p_y, from the SDF file provided by the EPOCH code. We provide the main details about this code in the Appendix. It filters the data outside the boxes where we derived the emittance and extracted the transversal positions and the momentum components. We then obtained their averages, considering also the particle weight, which was also extracted.

The vertical emittance is given by

$$\epsilon_y = \sqrt{\langle y^2\rangle \left\langle \frac{p_y^2}{p_x^2} \right\rangle - \left\langle y\frac{p_y}{p_x} \right\rangle^2}\,, \tag{3.2}$$

The results of the emittance and the average statistical parameters used in its formula showed a more compact electron bunch at higher modulation. We also obtained the Courant-Sneider parameters for these emittances, showing also a decrease in the phase space area for the lower emittances at higher modulation.

Thus, we performed a complete analysis of the LWFA mechanism in a modulated plasma density, starting from an analytical model for deriving the electron acceleration, then computing the depletion and dephasing lengths and investigating the betatron oscillations and the emittance of the electron bunches.

4 Conclusions and overview

In conclusion, this thesis aimed to provide an extensive description of laser wakefield acceleration and phenomena related to it, especially radiation emitted by the accelerated electrons. We described the laser-plasma interaction, the laser wakefield acceleration mechanism, the radiation emission by accelerated charges, and the computational PIC algorithm to model this dynamic.

We also presented our contributions to the literature, starting with the optimization of the PIC simulations and studying the proper grid parameters to obtain accurate electron energy output and reduce the computational resources used. We then described the dynamics of the electron trajectories forming the bubble, using a relativistic central field approach and observed the different geometries of the bubble closing. In the next study, we investigated how different plasma densities make the bubble close differently and how this affects the electron injection and the betatron radiation. In the fourth study, we approached the LWFA in a modulated plasma density, derived a model of electron acceleration in the varying size bubble, and also the dephasing and depletion lengths. We then studied the betatron oscillations and electron bunch emittance in this regime and observed their particularities depending on the modulation parameter.

Thus, this constitutes a broad description of the main aspects of LWFA and its computational modelling, followed by the meaningful contributions that we provided in the literature.

Bibliography

[1] Toshiki Tajima and John M Dawson. "Laser electron accelerator". In: *Physical review letters* 43.4 (1979), p. 267.

[2] AA Vlasov. "On high-frequency properties of electron gas". In: *Journal of Experimental and Theoretical Physics* 8.3 (1938), pp. 291–318.

[3] Rareș Iovănescu. "Laser self-focusing in plasma with a Vlasov model". In: Accepted for publication in *Rom. J. Phys.* (2025).

[4] Kane Yee. "Numerical solution of initial boundary value problems involving Maxwell's equations in isotropic media". In: *IEEE Transactions on antennas and propagation* 14.3 (1966), pp. 302–307.

[5] Jay P Boris et al. "Relativistic plasma simulation-optimization of a hybrid code". In: *Proc. Fourth Conf. Num. Sim. Plasmas*. 1970, pp. 3–67.

[6] J-L Vay. "Simulation of beams or plasmas crossing at relativistic velocity". In: *Physics of Plasmas* 15.5 (2008).

[7] Adam V Higuera and John R Cary. "Structure-preserving second-order integration of relativistic charged particle trajectories in electromagnetic fields". In: *Physics of Plasmas* 24.5 (2017).

[8] T Zh Esirkepov. "Exact charge conservation scheme for particle-in-cell simulation with an arbitrary form-factor". In: *Computer Physics Communications* 135.2 (2001), pp. 144–153.

[9] Alexander Pukhov. "Three-dimensional electromagnetic relativistic particle-in-cell code VLPL (Virtual Laser Plasma Lab)". In: *Journal of plasma physics* 61.3 (1999), pp. 425–433.

[10] TD Arber et al. "Contemporary particle-in-cell approach to laser-plasma modelling". In: *Plasma Physics and Controlled Fusion* 57.11 (2015), p. 113001.

[11] Rareș Iovănescu et al. "Optimisation of particle-in-cell simulations for laser wakefield acceleration". In: *University Politehnica of Bucharest Scientific Bulletin - Series A-Applied Mathematics and Physics* 85.1 (2023), pp. 159–166.

[12] Alexey V Arefiev et al. “Temporal resolution criterion for correctly simulating relativistic electron motion in a high-intensity laser field”. In: *Physics of plasmas* 22.1 (2015), p. 013103.

[13] Rareș Iovănescu et al. “Electron dynamics in a relativistic central field approach associated with laser acceleration of electrons”. In: *Rom. J. Phys.* 69.7-8 (2024), p. 501.

[14] Rareș Iovănescu et al. “Electron Filament Structures of Injected Electrons in LWFA”. In: *IEEE Transactions on Plasma Science* 53.4 (2025), pp. 780–787.

[15] Rareș Iovănescu et al. “Laser wakefield electron acceleration in a periodically modulated plasma density profile”. In: Submitted for publication in *IEEE Transactions on Plasma Science* (2025).